ELSEVIER

Journal of Power Sources 96 (2001) 303–320

JOURNAL OF POWER SOURCES

www.elsevier.com/locate/jpowsour

Computational fluid dynamics study of phosphotungstic acid electrolyte-based fuel cell (PWAFC)

Igor Lavrič[a,1], Pietro Staiti[b], Peter Novak[a], Stanko Hočevar[c,*]

[a]*Faculty of Mechanical Engineering, University of Ljubljana, Aškerčeva 6, SI-1000 Ljubljana, Slovenia*
[b]*Institute CNR-TAE, Via Salita S. Lucia sopra Contesse 5, IT-98126 S. Lucia, Messina, Italy*
[c]*Laboratory of Catalysis and Chemical Reaction Engineering, National Institute of Chemistry, Hajdrihova 19, P.O. Box 3430, SI-1001 Ljubljana, Slovenia*

Received 3 July 2000; received in revised form 9 October 2000; accepted 17 October 2000

Abstract

The computational fluid dynamics (CFD) study of the mass and heat transfer in the phosphotungstic acid electrolyte-based fuel cell (PWAFC) was performed in order to elucidate the cause of irregular fuel cell work failures at high current densities, which manifested through partial melting of the matrix and electrodes and crossover effect. It was established that the reason for these difficulties is not the damage (cracks) of the catalyst layer in the gas diffusion electrode, but the bad construction of the reactant gas and liquid electrolyte distributors on cathode and anode side of the PWAFC and the lack of cooling system. The CFD study pointed to several practical conclusions how to improve the PWAFC construction.

Keywords: Computational fluid dynamics; Fuel cell; Design; Mass and heat transfer; Phosphotungstic acid

1. Introduction

A low-temperature hydrogen/oxygen fuel cell has been developed recently, based on the concentrated aqueous solution of phosphotungstic acid (PWA) as proton conducting electrolyte [1,2]. Previous attempts to use PWA as a solid proton conducting electrolyte in crystalline form had failed in spite of its high proton conductivity (0.18 S cm^{-1}) at room temperature and high relative humidity of surrounding atmosphere [3–6]. The solid PWA electrolyte must be kept in its most hydrated crystalline form ($H_3PW_{12}O_{40}{\cdot}29$–$30$ H_2O), which has high enough proton conductivity (0.17 S cm^{-1}) to be applied in fuel cells [3]. This crystalline form exists only in the narrow interval of the high relative humidity. If the humidity drops below 80%, the conductivity of solid PWA drops by nearly an order of magnitude. On the other side, if the humidity approaches 100%, the phase of PWA changes abruptly from solid, crystalline electrolyte to the concentrated water solution of PWA, which has high proton conductivity (over 0.3 S cm^{-1} at 295 K) [7]. Moreover, the change of the PWA electrolyte phase occurs non-uniformly within the solid electrolyte in the working fuel cell while it depends on the current density distribution on the electrodes. The latter depends in its turn on the gas flow and distribution within the porous catalyst layer of the gas diffusion electrodes. The water management of the fuel cell with solid PWA electrolyte thus becomes a very demanding engineering task.

Since the idea to use PWA as the proton conducting electrolyte was originally founded on the ability of this electrolyte to modify the Pt electrode surface in such a manner that it becomes more resistant to transition metal ions poisoning [8] and to the CO poisoning [9] and that it enhances the kinetics of HER [10], we decided to continue the development of this new type of fuel cell even by using the PWA as liquid electrolyte in the form of concentrated aqueous solution. However, it was soon realized that the utilization of a traditional cell with the electrolyte flow parallel to the electrodes was not suitable for this type of electrolyte [7]. The high density and high dynamic viscosity of the concentrated PWA solution (60% PWA solution has a density of about 2 g cm^{-3} and dynamic viscosity of about 1.3 cP at room temperature) hinder its flow inside the porous matrix, creating high difference in PWA concentration between the fuel cell inlet and outlet points. Therefore, the through-flow configuration of the cell was developed with the flow of concentrated PWA solution in the direction from cathode to anode [2]. With this configuration we have

* Corresponding author. Fax: +386-1-425-92-44.
E-mail address: stanko.hocevar@ki.si (S. Hočevar).
[1] Present address: ZAG, Dimičeva 12, SI-1000 Ljubljana, Slovenia.

0378-7753/01/$ – see front matter
PII: S0378-7753(00)00655-8

successfully resolved also the problem of mixed potential created by electron conductivity of PWA via redox reaction [11]. Of course, the preparation of the gas diffusion electrodes had to be optimized for the use with the concentrated aqueous solution of PWA in order to create a proper three-phase interface in which the electrochemical reactions proceed [12]. The results obtained with this cell were encouraging. The 40 cm^2 cell with Pt loading of 0.5 mg cm^{-2} in gas diffusion electrodes working at room temperature and normal pressure was able to produce a maximum output power density of about 0.7 W cm^{-2} at current density 1.5 A cm^{-2} [1]. This performance was comparable to the laboratory performance of proton exchange membrane fuel cell (PEMFC) with Dow® membrane, having 0.4 mg cm^{-2} of Pt and working at 323 K and normal pressure [13].

Further development of the proof-of-the-concept fuel cell, based on concentrated liquid electrolyte, has manifested some serious drawbacks in the fuel cell operation: the loss of electrolyte through the outlet tubing of reactant gases and the excessive consumption of reactant gases with respect to their stoichiometric consumption in electrochemical reaction. Further post-mortem visual analysis showed zones in which the layers, electrodes and matrix, were dried and melted together due to hydrogen cross-over and hot spots formation on the surface of cathode and other zones where the electrodes and matrix appeared flooded with acid electrolyte. By these observations, it became evident that there were parts of electrodes and matrix assembly that operated under different fluid dynamic conditions. However, it was not possible to ascribe this damage of PWAFC components unambiguously to one reason. They could be a consequence of inappropriate procedure for fuel cell components assembling during which the small cracks in the catalyst layer of electrodes could be created and this would lead to the hydrogen crossover. But, they could also be created by inappropriate design of the reactant gases and liquid electrolyte flow patterns.

The complex problems of inappropriate fluid flow and distribution within the fuel cell can be resolved by using computational fluid dynamics (CFD) approach. This approach has an additional advantage: the detailed and comprehensive analysis can be applied to different fuel cell geometry and can be used simultaneously also for the resolution of heat transfer aspects of design. There are several examples of numerical simulation of fluid flow and heat transfer in fuel cells described in the literature [14–18]. Several two-dimensional models of fluid flow in PEMFC have been developed recently in order to elucidate the influence of the geometry of gas distributors and of porosity and thickness of diffusion layer of the gas diffusion electrode (mainly cathode) on the current distribution over the surface of the gas diffusion electrode [17–20]. With the advance of the PC computer performance the rather sophisticated software packages can be used to resolve engineering problems which would otherwise take to much time and efforts to be resolved experimentally [21].

In order to analyze the observed anomalies in the PWAFC performance, we decided to simulate the fluid flow and heat transfer in a complete 1:1 physical model of the PWAFC using CFD program PHOENICS, Version 2.2 for PC [22]. The results of the three-dimensional numerical simulation were validated through gas flow experiments performed in the cathode side half-cell configuration. The detailed analysis of the reactant gases flow and of the electrolyte flow as well as the analysis of heat transfer within the PWAFC are presented in this study. The conclusions were used to design PWAFC with better geometry.

2. Description of the PWAFC physical model

2.1. PWAFC geometry

This type of fuel cell configured as a through-flow porous catalytic plate reactor [2] is composed of several square or rectangular thin plates made of different electron conducting and insulating materials. This thin plate technology was used deliberately to simplify the production of all elements and the assembling of the fuel cell and fuel cell stack. On each electrode side there is one end plate with gas manifolds made of Plexiglas® with thickness of 1.0 cm, current collector plate made of expanded graphite with thickness 0.03 cm, two gas and electrolyte distributor plates made of expanded graphite each having thickness of 0.03 cm, a gas diffusion electrode composed of diffusion layer made of carbon paper (thickness 0.026 cm) and of catalytic layer made of hydrophobized Pt/C porous catalyst (thickness 0.01 cm), and an insulating porous matrix with liquid electrolyte hold-up having thickness of 0.026 cm. Superposition of these perforated layers creates two three-dimensional systems of channels for the flow of reactant gases and electrolyte, respectively. The overall surface of the PWAFC was 196 cm^2. The active surface of the electrodes was

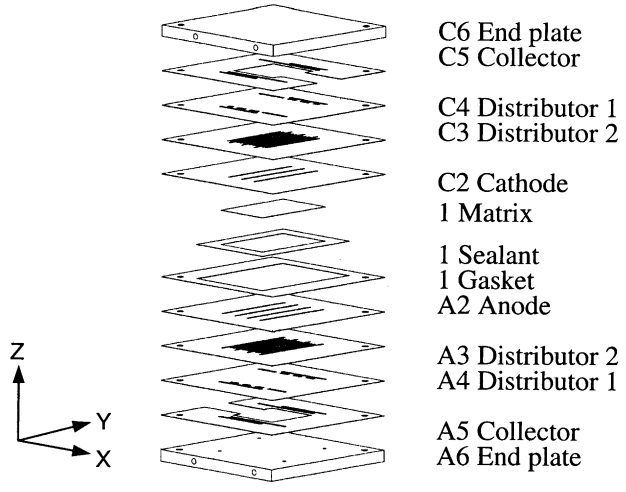

Fig. 1. The elements of the PWAFC (physical model).

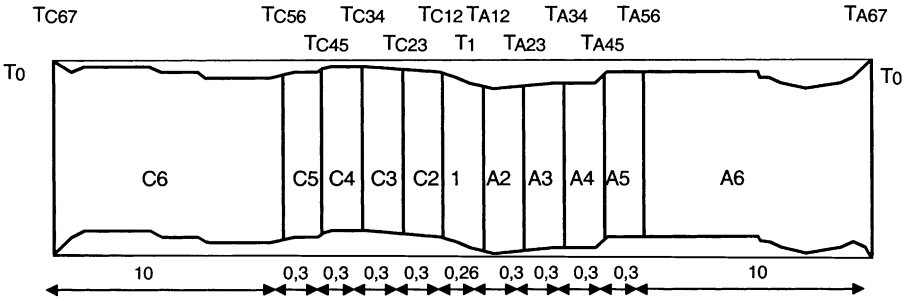

Fig. 2. Cross-sectional view of PWAFC. C*i* and A*i* are designations for cathode and anode side layers; T_{Cij} and T_{Aij} are designations for interfacial temperatures; the thickness of layers is given in mm.

36 cm^2 on each side. The expanded view of the PWAFC is shown in Fig. 1. The cross-sectional view with the designation of layers, their thickness and designation of interfacial temperatures is shown in Fig. 2. The thickness of the complete monocell between the end plates is 2.66 mm. The disposition of channels for electrolyte and gas flows on the distributor 2 at the cathodic side (see Fig. 1) is presented in Fig. 3 in order to facilitate the notion about reactant gases and electrolyte flow pattern in the through-flow configuration of the PWAFC. In this configuration the concentrated PWA solution is recirculated with low flow rate (1.0 $cm^3\ min^{-1}$) through the cell in direction from cathode to anode side.

2.2. PWAFC structure and materials

The end plates of the fuel cell were made of Plexiglas. The current collectors were made of goldened copper plates having thickness 0.25 mm and were placed into the cut area of the C5 and A5 collectors (see Fig. 1). The distributors were made of expanded graphite sheets (Papyex®, Le Carbonne Loraine, France). This material is anisotropic in thermal and electric conductivity: the thermal conductivity parallel to surface is $\lambda_{X,Y} = 11.1\ W\ m^{-1}\ K^{-1}$ and perpendicular to the surface is $\lambda_Z = 0.87\ W\ m^{-1}\ K^{-1}$; the electric conductivity parallel to the surface is $\sigma_{X,Y} = 1111\ S\ cm^{-1}$ and perpendicular to surface is $\sigma_Z = 4\ S\ cm^{-1}$ [23][2]. The carbon paper Toray TGP 090 having thickness of 0.27 mm, porosity $\varphi_s = 0.76$ and thermal conductivity $\lambda_s = 2.508\ W\ m^{-1}\ K^{-1}$ was used as a diffusion layer for gas diffusion electrodes preparation. The electric conductivity of this carbon paper is parallel to surface $\lambda_{X,Y} = 200\ S\ cm^{-1}$ and perpendicular to surface $\lambda_Z = 14.3\ S\ cm^{-1}$ [24]. The 0.1 mm thin catalyst layer was screen-printed on this carbon paper. The catalyst layer consisted of 20 wt.% Pt on active carbon hydrophobized with PTFE. The final Pt load in the electrode was 0.5 mg cm^{-2} [12]. The catalyst layer is composed predominantly of porous active carbon for which we take the thermal and electric conductivity data of graphite: thermal conductivity in the range between 112 and 188 $W\ m^{-1}\ K^{-1}$ and electric conductivity 15,385 $S\ cm^{-1}$ [25].

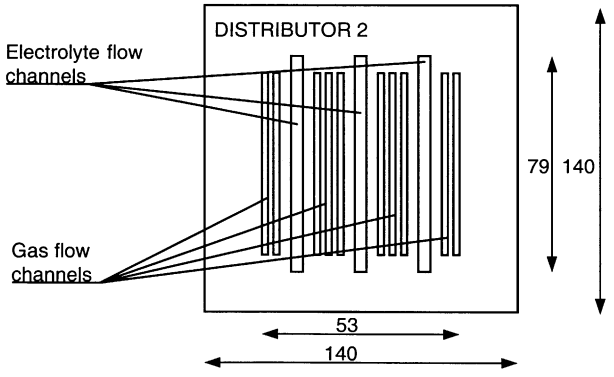

Fig. 3. The disposition of channels for electrolyte and gas flows on distributor 2 layer.

2.3. Description of fluid flow processes and conditions in the PWAFC

The reactant gases, hydrogen (H_2) and oxygen (O_2) are fed separately to the anode and cathode of the PWAFC, respectively. The gases first pass through the tubular channels of 3 mm i.d. in the end plates, then enter the right lower corner of each side into the current collector horizontal channel having a cross-section of 3 mm × 0.3 mm. They pass then through the horizontal perforation of the same cross-section in the first distributor plate and enter into the system of parallel vertical channels of the second distributor plate. The reactant gases flow thus along the diffusion layer of each gas diffusion electrode, diffuse freely into the catalytic layer and the gases in excess flow out at the upper left corner of each electrode side in the same manner as they entered the fuel cell, but in opposite direction.

The flow of liquid electrolyte (PWA) is in the direction from cathode to anode. The electrolyte enters the system of channels, made in essentially the same way as those for

[2] Alternatively, data for pure expanded flexible mineral graphite plain homogeneous gasketing sheets of Thermodynamics Asia Pacific Pte Ltd., Singapore (www.thermody.com/style7000pg1.htm) or Le Carbonne Loraine — Papyex® sheet characteristics.

reactant gases, at the left lower corner of the cathode. When the electrolyte flow reaches the gas diffusion cathode, it flows through the channels directly into the porous inert matrix. Here it distributes by capillary forces within the matrix and within the catalytic layer of both electrodes. The electrolyte comes out at the right upper corner of the anode. The flow of electrolyte through the porous inert matrix is limited. Therefore, the electrolyte in excess is allowed to come out at the upper left corner of the cathode.

The two systems of channels are completely isolated. The reactant gases and electrolyte come together only in the catalyst layer of both gas diffusion electrodes, where they form a subtly equilibrated three-phase contact in which the electrochemical reactions proceed.

The maximum work output in the form of electrical energy of the ideal H_2/O_2 fuel cell operating at constant temperature and pressure is given by the change of the Gibbs free energy of the overall reaction between H_2 and O_2:

$$W_{\max}^{\mathrm{el}} = \Delta G_{\mathrm{r}} = E_{\max} n N_0 e \tag{1}$$

where $E_{\max}$ is the reversible cell potential, n the number of moles of electrons transferred per mole of fuel consumed ($n = 2$ in this case), $N_0 = 6.023 \times 10^{23}$ e mol^{-1} (Avogadro's number), and $e = 1.6021 \times 10^{-19}$ C e^{-1} is the electric charge of electron. The product $N_0 e = F = 96{,}487$ C mol^{-1} e^{-1} is the Faraday's constant. Then

$$E_{\max} = -\left(\frac{\Delta G_{\mathrm{r}}}{n}\right) F = 1.229\ \mathrm{V} \tag{2}$$

at 298 K and 1 bar. The reversible cell potential is given by the Nernst equation:

$$E = E_0 + \left(\frac{RT}{2F}\right) \ln\left(\frac{a_{\mathrm{H_2}} (a_{\mathrm{O_2}})^{1/2}}{a_{\mathrm{H_2O}}}\right) \tag{3}$$

It is obvious from Eq. (3) that the cell potential increases with an increase in the activity of reactant gases and with a decrease in the activity of products. When the activity of gases is less than 1, the second term in Eq. (3) is negative. This means that with the increase of temperature the equilibrium cell potential will decrease and so will the maximum electrical work output. Therefore, if the electrochemical reaction kinetics permits, one should be interested to work at low temperatures in order to obtain more electrical work output. However, in practice the fuel cell voltage is much lower than the equilibrium Nernst potential since there are several irreversible losses connected with the existence of the over-potentials. The fuel cell voltage can thus be expressed with the following equation:

$$V = E - \eta_{\mathrm{act}} - \eta_{\mathrm{diff}} - \eta_{\mathrm{cond}} \tag{4}$$

where η_{act} is the activation over-potential, η_{diff} the diffusion over-potential and η_{cond} is the cell conductivity over-potential. These sources of the losses in the fuel cell voltage are not the only ones. There are several other losses on the level of the fuel cell system. All these losses can be expressed through

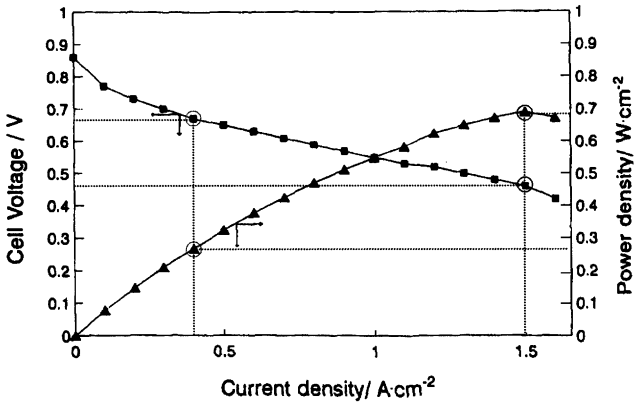

Fig. 4. Polarization curve for the PWAFC at 298 K and 1 bar H_2–O_2 gas pressure and the power density as a function of current density [1].

different efficiencies [26]. Three of them are of utmost importance for the practical fuel cell development:

- thermal efficiency $\varepsilon_{\mathrm{th}} = \Delta G_{\mathrm{r}} / \Delta H_{\mathrm{r}}$ (Gibbs free energy change/enthalpy change);
- voltage efficiency $\varepsilon_V = V/E$ (actual cell voltage/thermodynamic cell voltage);
- current efficiency $\varepsilon_I = \varepsilon_{\mathrm{F}} U$ (actual current/current equivalent of reactant molar flow rate),

where ε_{F} is the current efficiency at $U = 1$, and U is fuel utilization factor ($U = 0 \div 1$). The electrochemical efficiency of the fuel cell is then given as

$$\varepsilon_{\mathrm{E}} = \varepsilon_{\mathrm{th}} \varepsilon_V \varepsilon_{\mathrm{F}} U \tag{5}$$

For the numerical simulation of the fluid dynamics and heat transfer we have used the experimental data measured at the peak power conditions of the PWAFC [1] as the input values shown in Fig. 4. The values of these parameters are current density ($i = 1.5$ A cm^{-2}), cell voltage ($U = 0.47$ V) and electric power density output ($P_{\mathrm{el}} = 0.7$ W cm^{-2}). The fuel utilization in the numerical simulation was considered to be 1.0 ($U = 1.0$). It was assumed that fuel and oxygen are consumed at their stoichiometric ratio to form water. Therefore, $\varepsilon_I = \varepsilon_{\mathrm{F}} U = 1.0$. The theoretical maximum reversible potential of the H_2/O_2 fuel cell at room temperature (300 K) and normal pressure (1 bar) is $U_0 = 1.229$ V at the theoretical maximum value of the free enthalpy change $\Delta G_{\mathrm{r}}^0 = -237.2$ kJ mol^{-1}, and the reaction enthalpy change $\Delta H_{\mathrm{r}}^0 = -285.8$ kJ mol^{-1}, that is equal to the high heating value (HHV) of the fuel [26]. The experimentally obtained voltage at peak power density was 0.47 V. From these values we obtain for voltage efficiency $\varepsilon_V = V/E = 0.47/1.229 = 0.38$, and for the thermal efficiency $\varepsilon_{\mathrm{th}} = \Delta G_{\mathrm{r}} / \Delta H_{\mathrm{r}} = (-237.2)/(-285.8) = 0.83$. The electrochemical efficiency of PWAFC at peak power conditions is then calculated, according to Eq. (8) to be $\varepsilon_{\mathrm{E}} = 0.317$ or 31.7%.

Taking into account the efficiency at peak power conditions, we can calculate molar flow rates for fuel and

oxidant:

$$\dot{n}_H = \frac{AP_d}{\Delta H_r^0 \varepsilon_E} = \frac{36.34 \times 0.7}{-285.8 \times 10^3 \times 0.317} = 2.80 \times 10^{-4}\,\text{mol s}^{-1} \quad (6)$$

$$\dot{n}_O = \tfrac{1}{2}\dot{n}_H = 1.40 \times 10^{-4}\,\text{mol s}^{-1} \quad (7)$$

The corresponding mass and volume flow rates for hydrogen and oxygen at pressure $p = 1$ bar are $\dot{m}_H = 5.64 \times 10^{-4}$ g s^{-1}, $\dot{V}_H = 6.99$ cm^3 s^{-1}, $\dot{m}_O = 4.48 \times 10^{-3}$ g s^{-1}, and $\dot{V}_O = 3.49$ cm^3 s^{-1}, respectively.

Before numerical modeling, flow conditions in fuel cell have to be determined. Since the geometry of PWAFC is known in advance (see Section 2.1), we have checked for critical cross-sections in the system of channels for gas flow. The narrowest part of the hydrogen and oxygen inlet channels has a rectangular cross-section: width 3 mm and height 0.3 mm. The hydraulic diameter for this cross-section is calculated $D_h = 0.545$ mm. The average linear velocities of hydrogen and oxygen through this cross section are $\bar{v}_H = 7.77$ and 3.88 m s^{-1}, respectively. The Reynolds number for the flow of hydrogen would then be

$$Re_H = \frac{\bar{v}_H D_h}{v_H} = \frac{7.77 \times 0.545 \times 10^{-3}}{111 \times 10^{-6}} = 38 \ll 2320 \quad (8)$$

and for oxygen $Re_O = 131 \ll 2320$. It is obvious that even at the highest flow rate through the critical cross-section the Reynolds number is in both cases deep in laminar flow type region, therefore these findings are applied in numerical model solution procedure. In this evaluation we have presupposed that the inlet gas is not consumed in the electrochemical reaction ($U = 0$), so that the gas flow is maximal. In practice the fuel utilization factor was $U = 0.66$.

After describing the flow of reactant gases in the PWAFC, we shall describe now the flow characteristics of the liquid electrolyte — a 60 wt.% water solution of $H_3PW_{12}O_{40}$. In our through-flow configuration of the PWAFC the concentrated electrolyte enters the fuel cell on the cathode side, flows through the cell, as schematically shown in Fig. 5, and comes out diluted with the electrochemically formed water on the anode side. The concentrated electrolyte was pumped through the cell with a flow rate of 1 cm^3 min^{-1}. The molar and the mass flow rates of the electrochemically-produced water are calculated from the molar flow rates of the reactants. The molar flow rate of water is equal to the molar flow rate of hydrogen, when the fuel utilization factor $U = 1.0$.

The mass and volume flow rates of produced water are

$$\dot{m}_w = \dot{m}_H + \dot{m}_O = \dot{n}_H M_{H_2O} = 2.80 \times 10^{-4} \times 18 = 5.04 \times 10^{-3}\,\text{g s}^{-1} \quad (9)$$

and $\dot{V}_w = 5.05 \times 10^{-3}$ cm^3 s^{-1}. The mass and volume flow rates of the electrolyte are calculated as follows:

$$\dot{V}_E = 1\,\text{cm}^3\,\text{min}^{-1} = 1.66 \times 10^{-2}\,\text{cm}^3\,\text{s}^{-1} \quad (10)$$

$$\dot{m}_E = \dot{V}_E \rho_E = 1.66 \times 10^{-2} \times 2.0 = 3.33 \times 10^{-2}\,\text{g s}^{-1} \quad (11)$$

where $\rho_E = 2.0$ g cm^{-3} is the density of a 60 wt.% PWA solution at 298 K [7]. The specific heat of the electrolyte solution is $c_E = 3.4$ kJ kg^{-1} K^{-1} and its thermal conductivity is $\lambda_E = 0.7$ W m^{-1} K^{-1}.

2.4. Description of the heat transfer processes and conditions in the PWAFC

In the heat transfer part of the model we encounter several different types of heat transfer mechanisms such as conduction, convection, diffusion and radiation. We also encounter several types of material secondary structure: porous and non-porous solids, liquids, electric conductors and insulators. The most complex is the heat transfer through porous medium like gas diffusion electrode. In our case the gas diffusion electrodes were made of 0.3 mm thin carbon paper with porosity $\varphi = 0.76$ on which the 0.1 mm thin porous catalyst layer was screen-printed. The heat conductivity of porous medium can be estimated as the geometric mean value of the heat conductivity of solid (λ_s) and of the liquid filling the pores (λ_f):

$$\lambda_G = \lambda_s^{1-\varphi} \lambda_f^{\varphi} \quad (12)$$

This approximation holds when the λ_f is not much higher than λ_s. The heat conductivity values for hydrogen, oxygen and for the carbon paper are 0.183, 0.0268 and

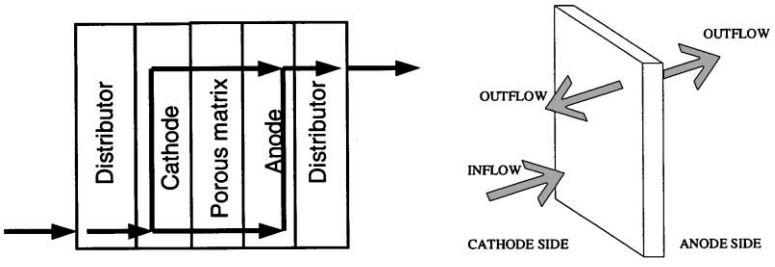

Fig. 5. Schematic representation of the electrolyte flow within PWAFC.

0.180 W m^{-1} K^{-1}, respectively. We calculate the heat conductivity for anode $\lambda_G = 0.182$ W m^{-1} K^{-1} and the heat conductivity for cathode $\lambda_G = 0.0423$ W m^{-1} K^{-1}. One can notice that the heat conductivity of hydrogen and that of anode material are very similar, therefore, the real structure of anode material is not important.

The heat flow which is generated during the fuel cell operation can be calculated from the peak power density and the electrochemical efficiency of the PWAFC:

$$\dot{q}''_g = \frac{P_{el}(1-\varepsilon_{el})}{\varepsilon_{el}} = \frac{0.7\times10^{-4}\times(1-0.317)}{0.317} = 1.51\times10^{-4}\,\mathrm{W\,m^{-2}} = 1.51\,\mathrm{W\,cm^{-2}} \quad (13)$$

This heat is generated as a Joule heat due to electrolyte resistance and as the electrochemical reaction heat in the three-phase region of the cathode catalyst layer. To calculate the specific volume heat generation, which one needs to define boundary conditions for the solution of numerical model, one must first calculate the active volume in which the heat is generated. The active surface of the anode is 36.34 cm^2 and the thickness of the inert matrix with liquid electrolyte holdup is 0.26 mm. The thickness of the three-phase electrochemical reaction region is in the order of 10^{-5} mm and can be neglected. Thus, the active volume for heat generation is $V_A = 0.9448$ cm^3, the specific volume heat generation is $\dot{q}''_g = 55.08\,\mathrm{W\,cm^{-3}}$ and the absolute value of the produced heat flow is $\dot{Q}_g = 54.87$ W.

The diffusion heat flow is generated when the laminar flow of reactant gas (H_2 or O_2) passes along the outer surface of the GDE diffusion layer while the reactant gas is consumed in the electrochemical reaction occurring within the catalyst layer of the GDE which adheres to the diffusion layer.

In the case of our model, the fuel utilization factor is $U = 1$ and the diffusion flows of the reactant gases in both electrodes are equal to their mass flows. We calculated these mass flows from the peak power conditions of the PWAFC. From these data we calculate the inlet enthalpy flows of both reactants: $\dot{H}_H = \dot{m}_H c_{p,H} T_H$ and $\dot{H}_O = \dot{m}_O c_{p,O} T_O$.

The heat transfer occurs also by the flow of liquid electrolyte through the fuel cell. Although the mass flow of liquid electrolyte is low, its specific heat is much higher than that for gases. The inlet enthalpy flow of electrolyte is

$$\dot{H}_{e,i} = \dot{m}_e c_e T_{e,i} \quad (14)$$

and the outlet enthalpy flow is

$$\dot{H}_{e,o} = \dot{m}_e c_e T_{e,o} + \dot{m}_w c_w T_{w,o} \quad (15)$$

One of the mechanisms for heat transfer in the PWAFC is also conduction in the expanded graphite sheets. This material exhibits anisotropy in both electric and heat conductivity. In such a case, a three-dimensional model for stationary heat conduction in the anisotropic medium is used (Fourier law). Since for expanded graphite $\lambda_X = \lambda_Y = 11.1$ W m^{-1} K^{-1} $\gg \lambda_Z = 0.87$ W m^{-1} K^{-1} one can use the simplified three-dimensional model in which the temperature in lateral directions changes faster than in perpendicular direction of the expanded graphite sheet, in accordance with difference in heat conductivity.

The linear velocities of electrolyte through cathode and anode are calculated from the electrolyte flow rate through the electrolyte channel cross-section and they are equal to $v_{e,z,C} = 0.267$ mm s^{-1} and $v_{e,z,A} = 0.352$ mm s^{-1}, respectively. These linear velocities of electrolyte are low, therefore, we shall pre-suppose that we have a standstill layer of electrolyte, having heat conductivity $\lambda_e = 0.7$ W m^{-1} K^{-1} and we shall treat the heat transfer in the electrolyte as a pure heat conduction.

The heat transfer from the surface of the electrode to the gas stream is calculated using the following procedure. The laminar flow in the channel of rectangular cross-section is considered to be fully developed. For the rectangular cross-section with sides ratio 5:1 (width of the channel $a = 1.5$ mm, height of the channel $b = 0.3$ mm) and the hydraulic diameter $D_h = 0.5$ mm the value of the Nusselt criteria would be $Nu_D = 5.75$ [23]. The heat transfer coefficient is then calculated for anode (H) and cathode (O) with the following equation:

$$\alpha_H = \frac{Nu_D \lambda_H}{D_h} = \frac{5.75\times0.183}{5\times10^{-4}} = 2104.5\,\mathrm{W\,m^{-2}\,K^{-1}} \quad (16)$$

and similarly $\alpha_O = 308.2$ W m^{-2} K^{-1}.

The heat flow with transfer from backside of electrode to the gas stream is defined as

$$\left(\tfrac{1}{2}\dot{q}_g\right) = \alpha A_{PC}(T_{C23} - T_O) \text{ for the cathode} \quad (17)$$

and

$$\left(\tfrac{1}{2}\dot{q}_g\right) = \alpha A_{PA}(T_{A23} - T_H) \text{ for the anode} \quad (18)$$

where, T_{C23} (K) and T_{A23} (K) are the temperatures at the interfaces schematically presented in Fig. 6.

The radiative heat transfer in the rectangular (1.5 mm × 0.3 mm) channels with view factor 0.01 between horizontal and vertical sides is so low that one can neglect it and take into consideration only radiative heat transfer between two parallel surfaces of layers:

$$\dot{Q}_R = \sigma_R A_P \frac{1}{(1/\varepsilon_1) + (1/\varepsilon_2) - 1}(T_{34}^4 - T_{23}^4) \quad (19)$$

Emitivities for electrode (carbon paper, $\varepsilon_1 = 0.95$) and distributor (expanded graphite, $\varepsilon_2 = 0.95$) materials, the value of Stefan–Boltzmann constant ($\sigma_R = 5.67\times10^{-6}$ W m^{-2} K^{-4}) and T_{34} (K) is either T_{C34} or T_{A34} (see Fig. 6), and T_{23} (K) is either T_{C23} or T_{A23} (see Fig. 6).

Although we have developed the mathematical model of heat transfer in the PWAFC we decided to find numerical rather than analytical solution, due to the complex three-dimensional geometry of the fuel cell. For this purpose we have used the CFD software package PHOENICS [22].

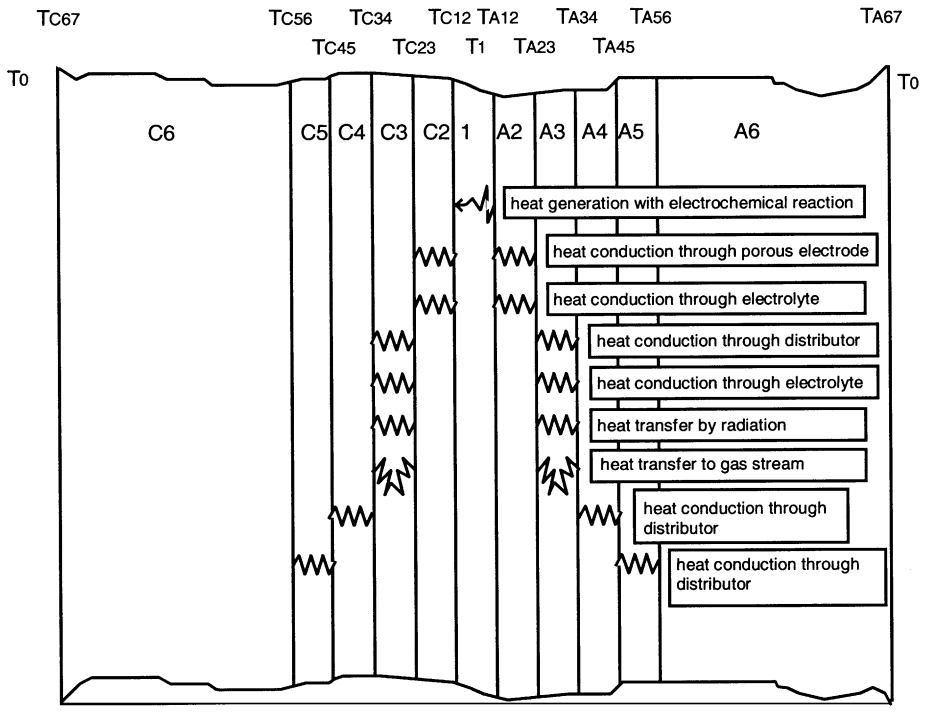

Fig. 6. The scheme of heat transfer mechanisms in the PWAFC.

3. Numerical model of the PWAFC

In the previous section we have described the physical model of the PWAFC and the processes and conditions during its work which enable the definition of boundary conditions for numerical modeling of mass and heat transfer processes within the fuel cell. The scope of this work was not to calculate accurate numerical values of physical parameters in one point, but rather to establish global relations and distributions of particular parameters through the entire fuel cell.

There are three main causes for the heat generation within the fuel cell:

1. Electrochemical (electrocatalyzed) reaction between mobile protons and adsorbed oxygen anions on the Pt catalyst of cathode.
2. Chemical (heterogeneously catalyzed) reaction between molecular hydrogen, crossing over from anode to cathode due to too high permeability of the membrane electrolyte or matrix filled with liquid electrolyte, and adsorbed oxygen on Pt catalyst in the cathode.
3. Ohmic resistance of the electrolyte (solid or liquid). The resistance of ionic conductors is roughly 1000 times higher than the resistance of electronic conductors. The heat generated in this way is proportional to the square of current passing the electrolyte (Joule heat).

The generation of heat within a fuel cell is a direct mapping of the distribution and consumption of reactant gases within the porous gas diffusion electrodes. But, since the distribution of reactant gases depends on the fluid (gases and electrolyte) dynamics within given fuel cell geometry, the study of heat generation in the fuel cell is closely related to the study of distribution and flow of fluids in it [19]. The mass flow of oxygen in the cathode and hydrogen in the anode is directly proportional to the current density. The square of current multiplied by internal resistance of the fuel cell (which is equal to the resistance of ionic conductor, i.e. electrolyte) represents the Joule heat.

Based on these facts we have approached to the study of heat flow by using the software package for modeling the fluid dynamics and heat transfer. The results obtained with numerical model on the reactant gas distribution in the gas diffusion electrodes (cathode and anode) are fully correlated with the heat generation in the fuel cell.

We have also performed the numerical simulation of the liquid electrolyte flow through the fuel cell since it regulates the formation of the three-phase region within the GDE catalyst layer where the electrochemical reactions proceed and since it regulates the liquid electrolyte specific conductance and Joule heat generation.

The combination of the gas flows and electrolyte flow numerical simulation within the PWAFC should give us the answer on the following question: under which simulated operating conditions of the PWAFC one can expect anomalies that we have encountered during experimental runs of PWAFC.

3.1. General description of numerical modeling procedure

The governing partial differential equations (PDEs) are solved for the conservation of mass, momentum, energy and

chemical species as applicable. The governing PDEs, each representing the continuity equation when $\phi = 1$, is written in the form of a Cartesian tensor as

$$\underset{\text{transfer term}}{\frac{\partial(r\rho\phi)}{\partial t}} + \underset{\text{convection term}}{\nabla(r\rho\phi\vec{v})} - \underset{\text{diffusion term}}{\nabla(r\chi\nabla(\phi))} = \underset{\text{source term}}{S} \quad (20)$$

where r is the volume part, ρ the density, ϕ the conserved mass, momentum, energy or species quantity, t the time, $\vec{v}$ the velocity vector, χ the transport coefficient (viscosity, heat conductivity, etc.), and S is the change of property.

Each PDE is reduced within PHOENICS software package to its finite volume form by integrating it over the control volumes of the design domain.

In the numerical calculation other additional equations are used which describe the thermodynamic properties (density, etc.), transport properties (viscosity, diffusion, convection, etc.), generating properties (radiation absorption, chemical generation, viscous dissipation, etc.) and also interface transport properties (moment, energy, etc.). The boundary conditions have to be set as a constant value of certain property, as a constant flux of certain property and as linearly and non-linearly defined properties.

3.2. Entry data

We have developed a three-dimensional model of the fuel cell in which the heat transfer proceeds by conduction and convection. The radiative heat transfer is negligibly small and omitted from the model because of the low fuel cell working temperatures (less than 353 K) and because of small temperature difference between the fuel cell layers in the perpendicular direction. Based on the preliminary estimation of the mass transfer conditions in the fuel cell (see Section 2.3), we have chosen the way of solving the numerical model, which is adapted for the laminar flow of the gases.

The whole model of the fuel cell is oriented as shown in Fig. 1, where the in-plane directions are *X*- and *Y*-, and the *Z*-direction is perpendicular to the plane. The geometrical model for numerical simulation is composed of nine individual layers, each having the thickness of 0.30 mm, with the exception of the middle layer representing the inert porous matrix with thickness of 0.26 mm. The outer dimensions of the model are, therefore, 140 mm in *X*-direction, 140 mm in *Y*-direction and 2.66 mm in *Z*-direction.

The porous elements of the fuel cell, such as both gas diffusion electrodes are set to a value of 0.76 of volume porosity. The numerical calculation of the model was divided into two parts:

1. the calculation of the oxygen flow through the gas channels on the cathode side;
2. the calculation of the electrolyte flow through the channels across the entire fuel cell.

In calculations of the first part we defined the electrolyte channels on the cathode side as filled blocks (standstill electrolyte). The oxygen flow for the given operation conditions of the fuel cell is known. The linear velocities and mass flow rates were calculated with regard to the inlet and outlet cross-sections, which are 24 mm^2 (3 mm × 8 mm).

The outlet cross-section had to be defined at the 0 kPa pressure. The proper sources for the heat generation were defined and the values of specific heat flow per unit volume were calculated.

3.3. Numerical calculations

The structured grid was developed based on the geometrical model of the fuel cell. The grid is composed of 130 × 58 × 21 (158340) nodes. These nodes are distributed across the *X*–*Y*-plane in such a way as to enable the continuous representation of computed results in all regions. In the regions containing the gas and electrolyte distribution channels the grid is denser. To reach the adequate accuracy limits in the next calculation step about 1000 iterations were necessary, which took more than 15 hours of processing time on a PC with Pentium 233 MMX.

4. Analysis of the numerical simulation results

4.1. Analysis of the numerical simulation results for the oxygen flow in the cathode side half-cell of PWAFC

The oxygen flow in the cathode side half-cell was calculated without heat generation. The pressure distribution and the velocity vectors were determined without the influence of the temperature. Four plains represent each layer within the cathode side half-cell. The velocity vectors and their components are presented separately for the distributors (left side) and for the porous cathode (right side) in Figs. 7–10. The calculated values of variables have the following designation:

P1	relative pressure (the value of surrounding pressure is 100 kPa) (Pa);
U1	velocity component in the *X*-axis direction ($m\ s^{-1}$);
V1	velocity component in the *Y*-axis direction ($m\ s^{-1}$);
W1	velocity component in the *Z*-axis direction ($m\ s^{-1}$);
Vector	velocity vector ($m\ s^{-1}$);
TEM1	absolute temperature (K).

The intensity for each represented variable is given in gray scale. In order to improve graphical visualization of each variable value the view in *Z*-axis direction is expanded 50 times. The left side of Figs. 7–10 represents the oxygen velocity distribution within the channels of the collector, distributors 1 and 2, and the right side of Figs. 7–10 represents the oxygen velocity distribution on the backside plane of the porous cathode.

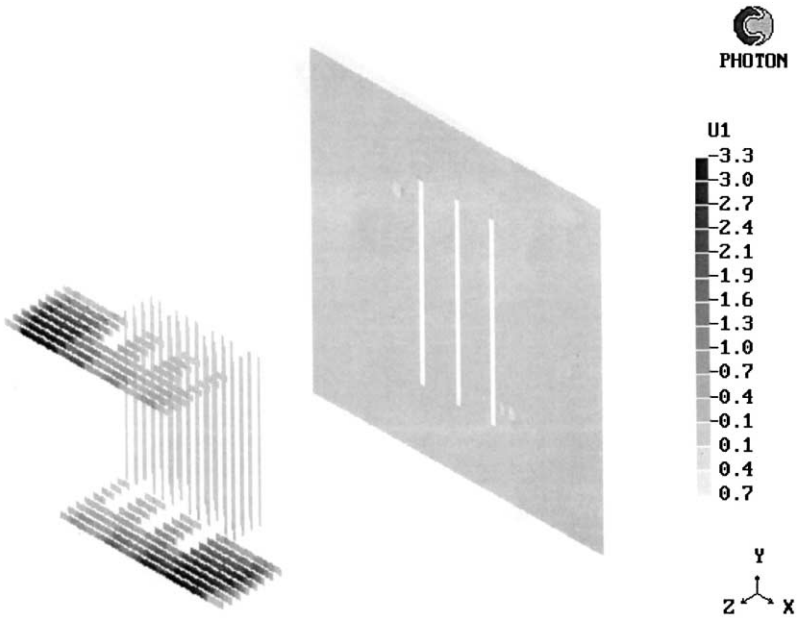

Fig. 7. *X*-axis component of oxygen flow velocity in the channels formed by superposition of collector, distributors 1 and 2 (left) and on the back surface of the cathode (right).

Fig. 7 (left side) reveals that the *X*-axis component of velocity is uniform along the height of the channel (3 mm), while it changes drastically along the width of the channel (0.6 mm). On the front wall of the channel it reaches 3.3 m s^{-1} and then it drops to nearly zero value on the back wall of the channel. One can notice that the velocity of oxygen flow along the channel rises and drops intermittently, according to the widening and narrowing of the channel formed by superimposed layers of collector and distributor 1 (see Fig. 1). The distribution of the *X*-axis velocity component in the upper outlet channel (the oxygen exits at the upper left corner) is nearly the same as that in the lower inlet channel, but rotated for 180° clockwise around the *Z*-symmetry axis.

The *Y*-axis component of the oxygen flow velocity distribution is shown in Fig. 8. In the distributor 2 vertical channels the highest positive values of this velocity compo-

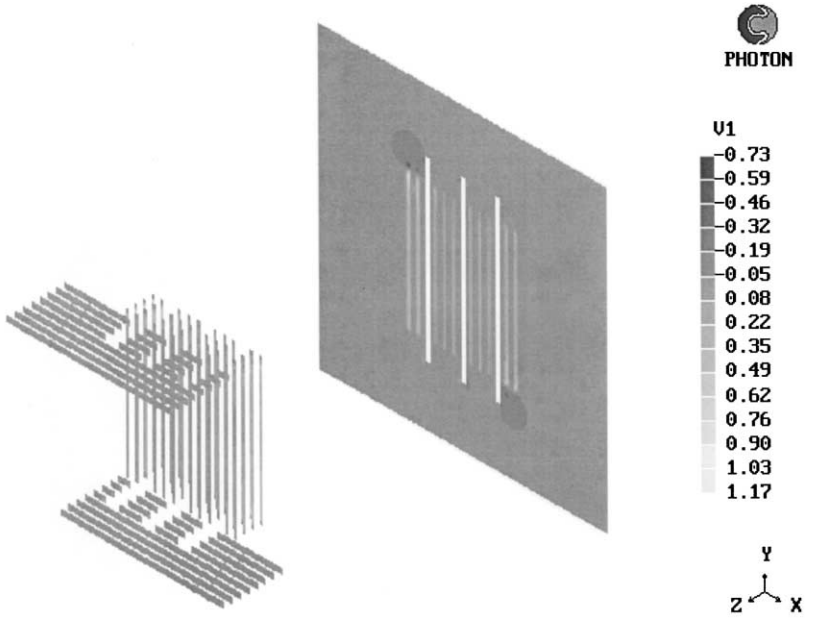

Fig. 8. *Y*-axis component of oxygen flow velocity in the channels formed by superposition of collector, distributors 1 and 2 (left) and on the back surface of the cathode (right).

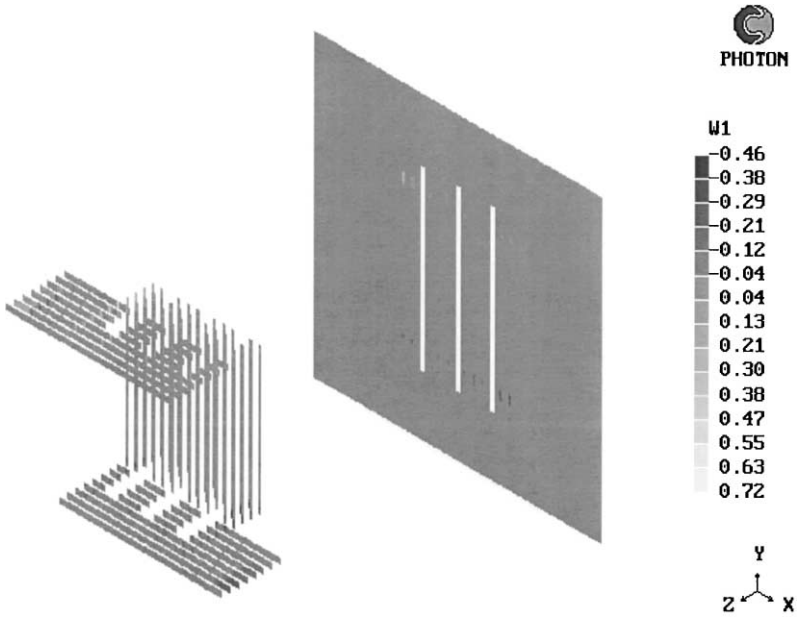

Fig. 9. *Z*-axis component of oxygen flow velocity in the channels formed by superposition of collector, distributors 1 and 2 (left) and on the back surface of the cathode (right).

nent, about 1 m s^{-1}, are achieved at the entrance into the first vertical channel and at the exit from the last vertical channel (Fig. 8, left). The *Y*-axis velocity component values on the backside surface of the cathode (Fig. 8, right) are the highest and positive in vertical stripes which match the position and geometry of the vertical distribution channels in the distributor 2.

Fig. 9 represents the distribution of the *Z*-axis gas velocity component in the cathode compartment of the PWAFC. One can notice that the non-zero values are located only at the points of oxygen inlet and outlet and the points of the vertical channel entrance and exit (Fig. 9, left).

The integral view of the oxygen flow in the cathode compartment is presented in Fig. 10 in the form of velocity

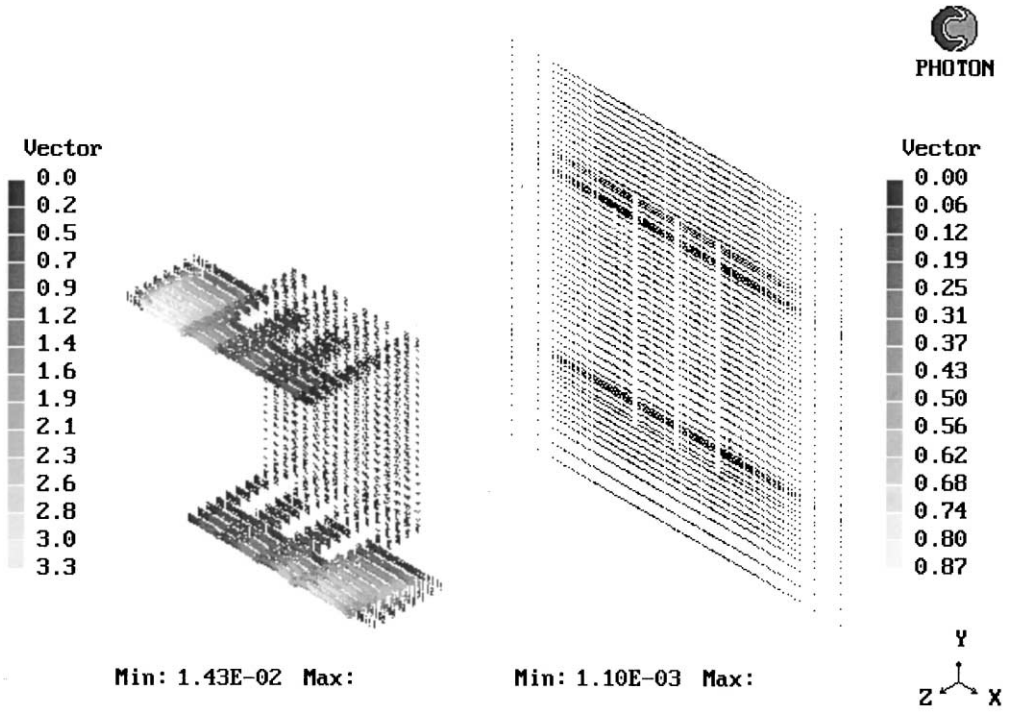

Fig. 10. Velocity vectors of oxygen flow in the cathode compartment of PWAFC.

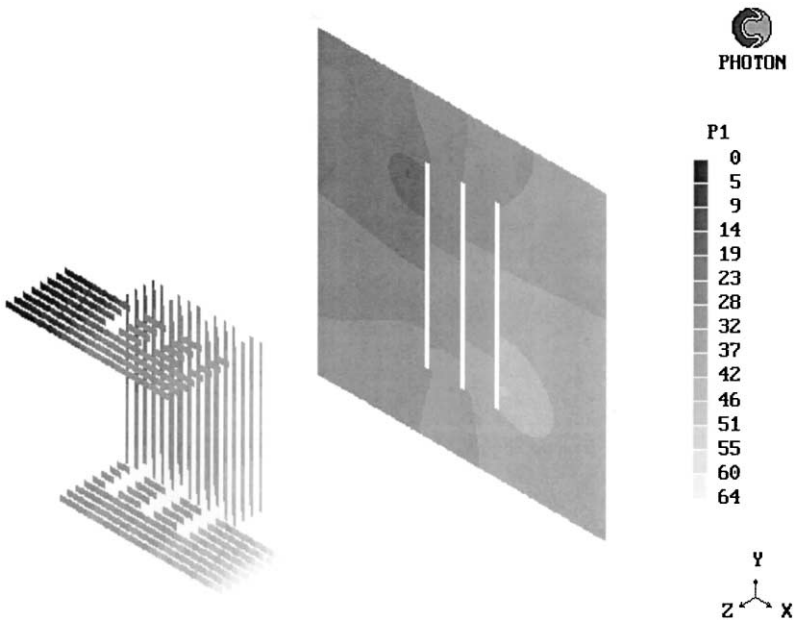

Fig. 11. The oxygen pressure field within the distribution channels of the cathode compartment (left) and on the backside surface of the cathode (right).

vectors. The maximum values of the velocity vectors within the channels (Fig. 10, left) are equal to the maximum values of the *X*-axis velocity component (compare with Fig. 7, left). The velocity vectors distribution on the backside surface of the cathode (Fig. 10, right) matches well the distribution of the *Y*-axis velocity component (compare with Fig. 9, right).

The pressure distributions along the channels (Fig. 11, left) and on the backside cathode surface (Fig. 11, right) give us the best visual presentation of the stationary oxygen flow conditions in the cathode compartment of the PWAFC. The overall pressure drop between the oxygen inlet point and the oxygen outlet point amounts 64 Pa (Fig. 11, left). One can notice that the pressure uniformly drops along the horizontal double-width channel from the inlet point to the point of entrance into the first two vertical channels. Here, the pressure somewhat rises due to the horizontal channel narrowing, and then continues to drop uniformly until the next branching off into the vertical channels. It is important to note that the pressure drop along the horizontal channel is about twice as large as the pressure drop along the vertical channels. The stationary picture of pressure drop on the backside surface of the cathode reflects the one in the last layer of the distributor 2, with the exception that the pressure field is spread over the entire surface of the cathode (Fig. 11, right). One can observe the stepwise pressure drops between the regions delineated by the vertical electrolyte-filled channels. These channels are impermeable for the gas in our numerical model. The values of these pressure drops along both sides of the vertical electrolyte filled channels are equal to the pressure drops in both horizontal distribution channels (lower inlet and upper outlet channel).

The analysis of the pressure field reveals that the highest pressure drops are generated within inlet and outlet horizontal gas distribution channels formed by superposition of the collector and distributor 1. The immediate practical conclusion can be drawn: the cross-section of these two channels should be increased and the obstacles created by intermittent narrowing and widening along these channels should be removed. Also, the gas inlet and outlet should be enabled on both sides of the horizontal channels.

4.2. Analysis of the numerical simulation results for the electrolyte flow within the PWAFC

The electrolyte flow within the entire fuel cell geometry was numerically modeled, but in this case the gas flow was excluded. The flow scheme of electrolyte is slightly different from that of the reactant gases. This flow pattern is shown in Fig. 5.

The volume flow rate of the electrolyte is low and in the model we took the value of 1 $cm^3\ min^{-1}$. No doubt, this flow is laminar, because the inlet linear velocity through the 9 mm^2 cross-sectional area is 1.856×10^{-3} m s^{-1}. The *X*-axis component of electrolyte flow velocity distribution within PWAFC is shown in Fig. 12 (left). These velocity component values are the highest in the horizontal inlet and outlet channels, and are equal to zero in the vertical channels and close to zero in the porous matrix. The highest values of the *X*-axis velocity component do not exceed 2×10^{-2} m s^{-1}. The *Z*-axis component of the electrolyte flow velocity distribution is also close to zero in the channels and in the porous matrix, as shown in Fig. 12 (right). However, the most interesting is the distribution of the *Y*-axis electrolyte velocity component in the vertical channels of the distributor 2 and of electrodes, and in the inert porous matrix with electrolyte holdup (Fig. 13). In the given upflow

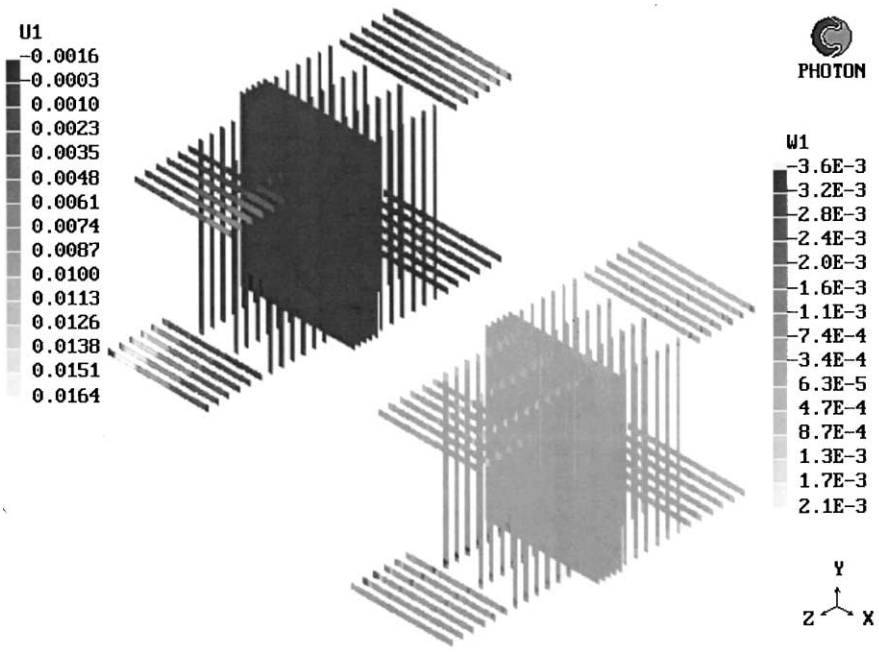

Fig. 12. The *X*-axis velocity component (left) and the *Z*-axis velocity component (right) of the electrolyte flow distributions.

configuration of the electrolyte circulation through the fuel cell, the electrolyte flow is divided: one part of electrolyte flows through porous matrix and exits through the upper horizontal channel on the anode side; the other part of the electrolyte flows upward the vertical channels in the cathode and upward the porous matrix and then exits through the upper horizontal channel on the same, cathode side.

As in the case of oxygen flow, the most illustrative representation of the stationary electrolyte flow conditions within the PWAFC is obtained by examining the pressure field (Fig. 14). The highest pressure is created at the inlet point of electrolyte flow which amounts to 5.4 Pa. Especially informative is the pressure field created in the porous inert matrix which determines the rate of electrolyte renewal within the three-phase region of the electrode catalyst layer that adheres to the porous matrix. This rate in turn determines the rate of the electrochemical reactions on both electrodes.

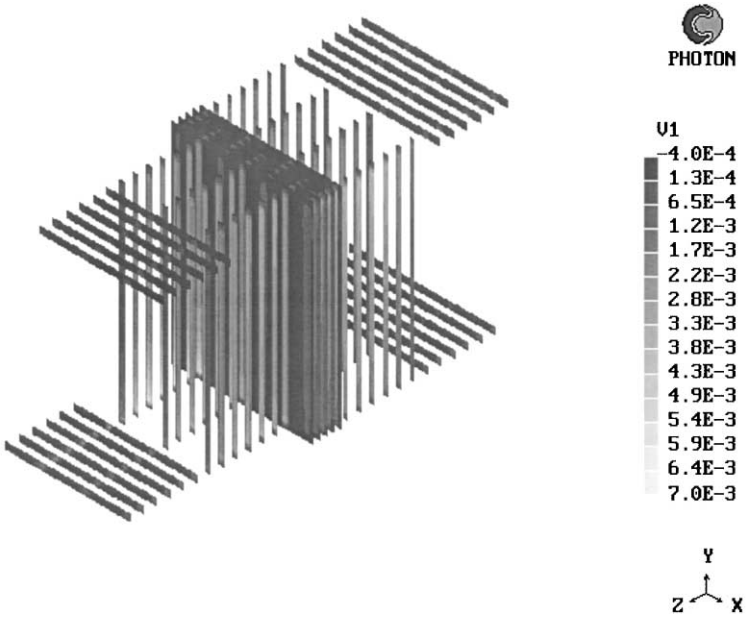

Fig. 13. The *Y*-axis velocity component of the electrolyte flow distribution.

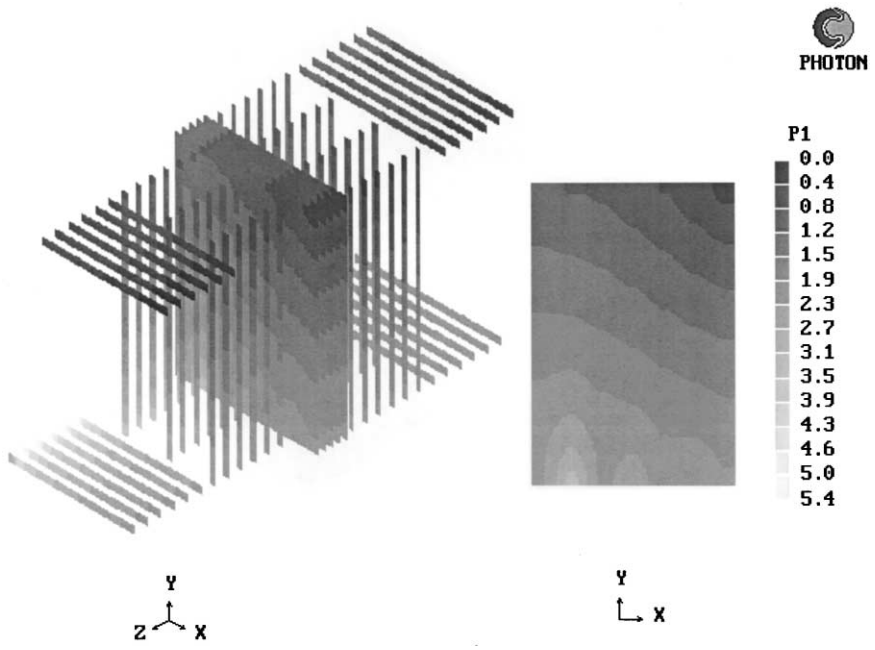

Fig. 14. Pressure field created by the electrolyte flow in the PWAFC (left) and in the inert matrix (right).

As can be seen in Fig. 14 (right) the created electrolyte pressure field within the porous matrix is far from being homogeneous. The ratio between the pressure drop along the horizontal distribution channel and along the vertical channels and in vertical direction of the matrix is lower than it was in the case of gas pressure drop in horizontal channels and in the vertical direction of the backside surface of the cathode.

When looking from the cathode side, the upper right corner of the matrix, and, on the same place also both electrodes, will be poorly wetted, while the diagonally positioned lower left corner of the matrix and of both electrodes will be wetted sufficiently. When one makes the superposition of the schematically represented pressure gradients of the electrolyte in matrix and of the gas (oxygen) in the cathode, the picture like the one represented in Fig. 15 emerges.

It is evident that the lower right corner of the catalyst layer on cathode will be well fed with oxygen, but will not be wetted enough with fresh electrolyte. The lack of electrolyte (or inhomogeneous electrolyte distribution) can cause several deteriorating effects. In such cases the electrolyte would be diluted faster with the electrochemically produced water and the local Ohmic resistance would increase. Consequently, the local temperature would also increase. This would imply local drying of the matrix. On the other side, the pressure of both gases is highest exactly at this point, and this creates favorable conditions for the hydrogen crossover with all possible deterioration consequences.

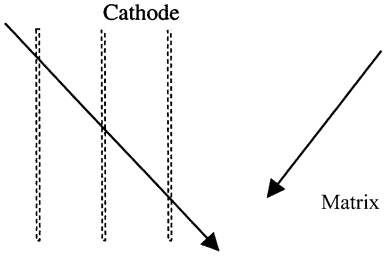

Fig. 15. Schematic representation of the pressure gradients of gas in the electrode and of electrolyte in the matrix.

4.3. Analysis of the temperature distribution in the PWAFC

The temperature distribution in the electrolyte and in the middle of the matrix filled with electrolyte was calculated for the following conditions:

- the cell works at the peak power conditions;
- the surrounding of the cell is adiabatic;
- the heat is generated uniformly at the cathode-side surface of the matrix;
- the cell is cooled only with the flowing-in electrolyte having the temperature of 293 K.

The temperature fields across the cell and in the central layer of the matrix resemble somewhat the analogous electrolyte pressure fields, as one would expect (Fig. 16). The contours of the position of the horizontal and vertical distribution channels for gas and electrolyte can be recognized in the temperature field of the matrix (Fig. 16, right). The temperatures along the vertical distribution channels for the electrolyte are somewhat lower than in the other places in the matrix. But, it is obvious that the circulation of the

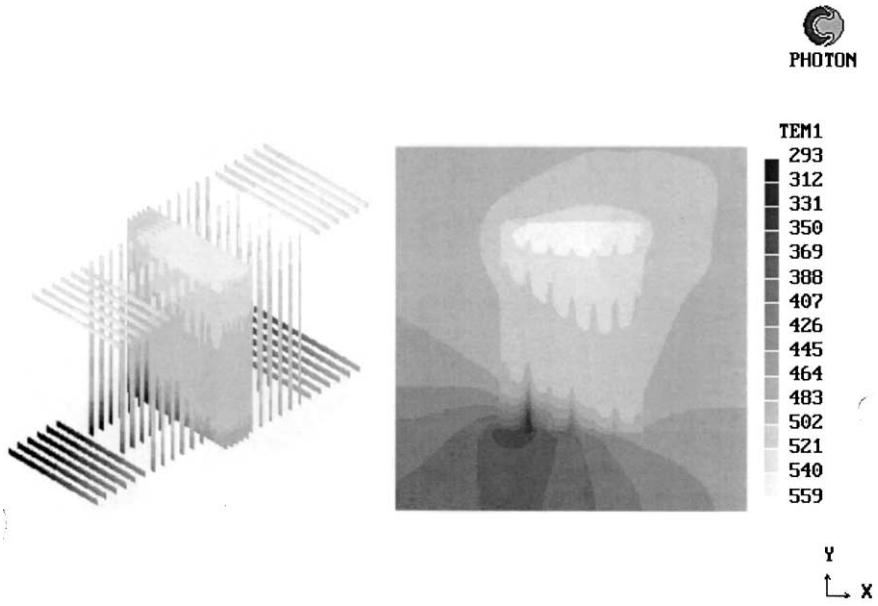

Fig. 16. The temperature distribution across the cell (left) and in the central matrix layer (right).

electrolyte alone does not suffice for effective cooling of the cell at the peak power conditions. In order to improve the cooling of the fuel cells within the fuel cell stack it would be necessary to introduce the heat exchangers with water as cooling medium. Only by introducing the effective cooling system one can assure the normal cell operating conditions that would prevent the temperature to rise above the water boiling point at the surrounding pressure.

5. Validation of the numerical model results by designed gas flow experiment

The original idea of numerical model validation was to design experiment in which the basic parameters of the fluid flow (the mass flows of reactant gases and of the electrolyte) and of the temperature distribution within the fuel cell would be measured continuously in PWAFC with given geometry and operational conditions. This would demand the measurement of temperature in the catalyst layer of the cathode and on the surface of other layers inside the PWAFC on at least 20 points. Such an experiment design brings about some inherent drawbacks like substantially diminishing the active surface of the cathode catalyst layer due to temperature sensors positioning, corrosion of the sensors and wiring, problems in assuring the tightness between layers containing temperature sensors, etc.

We decided, therefore, to simulate the development of the stationary flow conditions of oxygen in the cathode compartment of the PWAFC by assembling the cathode-side half-cell, putting the sheet of the whiteprint paper on the catalyst layer, covering it with a transparent Plexiglas® plate, and recording the time evolution of the coloring reaction of diazo dye when exposed to white light and a flow of ammonia. Since the flow characteristics of ammonia are close to those of oxygen and the whiteprint paper coloring reaction is fast, this experiment offers the fluid flow and chemical reaction conditions that approach most closely to the conditions of oxygen flow and the electroreduction of oxygen in the cathode compartment. On the other side the lateral temperature distribution in the cathode depends on the Joule heat generated within the fuel cell. The latter is proportional to the square of current density lateral distribution, which in its turn is directly proportional to the lateral distribution of oxygen mass flow within the porous medium of gas diffusion cathode. The dimensions of the particular layers in this half-cell are the same as those used in the geometry entry of the numerical model.

The whiteprint paper was mounted on the catalyst layer surface of the cathode and the half-cell was then closed by another transparent Plexiglas® end plate. The time evolution of the colored zone was filmed with the digital camera. The whole experimental installation is schematically represented in Fig. 17.

Simultaneously with the video recording and scanning of the time evolution of gas distribution on cathode, the flow rate of ammonia was measured with the soap bubble meter flow calibrator and the pressure drop of ammonia in the cathode compartment was measured with the U-manometer filled with Squalan ($\rho = 0.808\ \mathrm{g\ cm^{-3}}$). The experiments were performed at three values of ammonia flow rate: 5.5, 24.8, and 49.4 $\mathrm{cm^3\ min^{-1}}$ which are close to the nominal values used in the ammonia flow numerical simulations (5, 25 and 50 $\mathrm{cm^3\ min^{-1}}$). The estimated ammonia flow rate measurement uncertainty is around 1.1 $\mathrm{cm^3\ min^{-1}}$. The experimentally determined static pressure drops at three different ammonia flow rates were 8.9, 38.0 and 66.3 Pa. The estimated pressure drop measurement uncertainty was

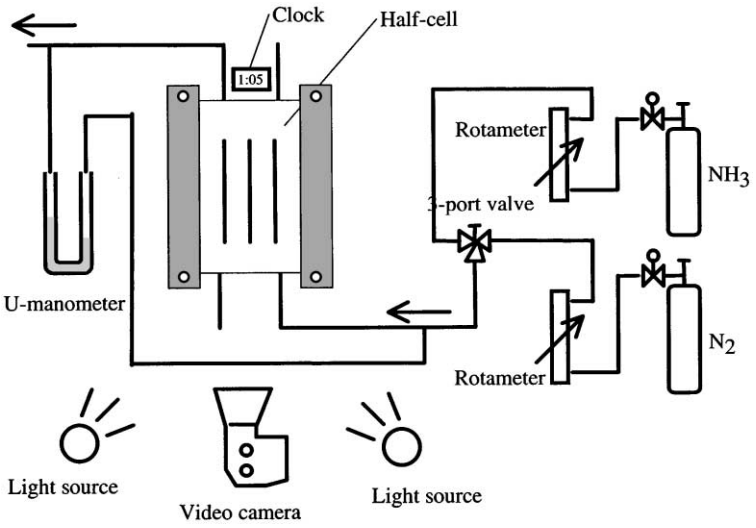

Fig. 17. The scheme of the experimental setup for measurements of the whiteprint paper coloration with ammonia.

4.04 Pa. In order to compare the experimental results with the results of numerical simulation, we have calculated also the dynamic pressure for the highest ammonia flow rate $P_d = 1.5 \times 10^{-3}$ Pa. The dynamic pressure at the inlet and at the outlet of the cathode compartment is low and we shall neglect it in our further discussion.

The video sequences acquisition was performed with FPS60 video card (Fast Multimedia, Germany) and Premiere software package (Adobe) [27]. The frequency of acquisition was one snapshot per second.

The pictures were then processed further on with a software package Picture Publisher 6.0 (Micrografx, USA) [28]. The contours obtained by processing the successive snapshots were then superposed in order to obtain one picture demonstrating the time evolution of the reaction front.

The measured and calculated flow characteristics of ammonia are linear (Fig. 18). Using the Darcy's equation for pressure drop for laminar flow we get the following equation of flow characteristic in the cathode compartment of the fuel cell, giving the linear relation between the gas velocity and pressure drop:

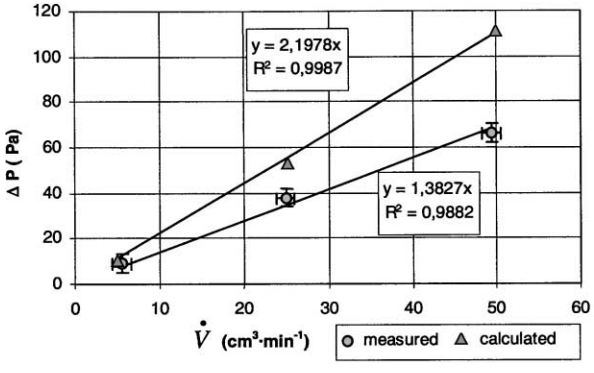

Fig. 18. Measured and calculated ammonia flow characteristics.

$$\Delta p = K v \rho \dot{V} = 98,676 \times v \rho \dot{V}\,(\mathrm{Pa}) \quad (21)$$

where for ammonia $v = 14.7 \times 10^{-6}\ \mathrm{m^2\,s^{-1}}$ and $\rho = 0.6894\ \mathrm{kg\,m^{-3}}$. One can notice that the measured and calculated values for pressure drop agree well in case I, that is at low ammonia flow rate. At higher flow rates the measured and calculated flow characteristics part and the calculated values are higher than measured ones. We ascribe this to enhanced leakage of ammonia from experimental assembly at higher pressure drops.

The time evolution of the reaction front measured at three different flow rates of ammonia through cathode compartment of the PWAFC is represented in Fig. 19. The coloring reaction front propagates faster along the first vertical channel (on the right side) and with time lags needed for the propagation along the horizontal channel (lower one) it then propagates also along the successive vertical channels (Fig. 19, case I). At higher ammonia flow rates the propagation of coloring reaction along the first vertical channel becomes increasingly faster comparing to the propagation along successive vertical channels. Ammonia from the first vertical channel reaches the upper horizontal channel and spreads along it faster than from successive vertical channels. Moreover, one can notice that the ammonia (and consequently the coloring reaction) propagates from the upper horizontal channel into the last two vertical channels downward! This creates the asymmetry in the propagation front of the coloring reaction visible in Fig. 19 (cases II and III). The propagation in the first vertical channel of case II is equal to the propagation in the second vertical channel of case III, since the flow rate in case III is doubled with respect to flow rate in case II. Detailed inspection reveals that the difference in the reaction propagation velocity along the first and second vertical channels increases with flow rate when the flow rates are high enough. This effect is represented in Fig. 20.

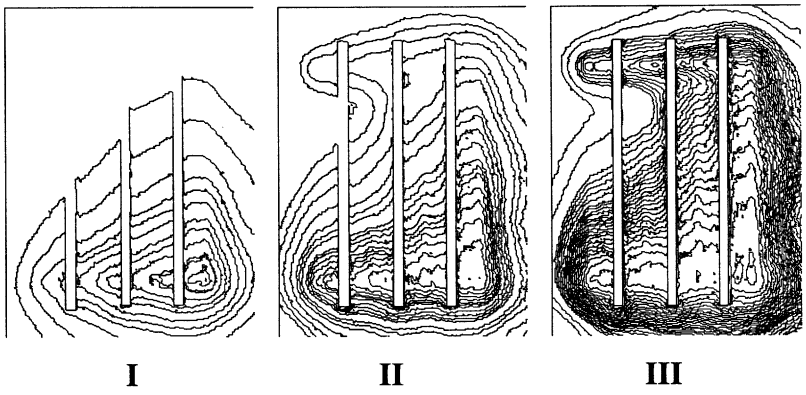

Fig. 19. The time evolution of the coloring reaction front on whiteprint paper at three values of ammonia flow rate through the cathode compartment: 5.5 $cm^3\ min^{-1}$ (I); 24.8 $cm^3\ min^{-1}$ (II); 49.4 $cm^3\ min^{-1}$ (III).

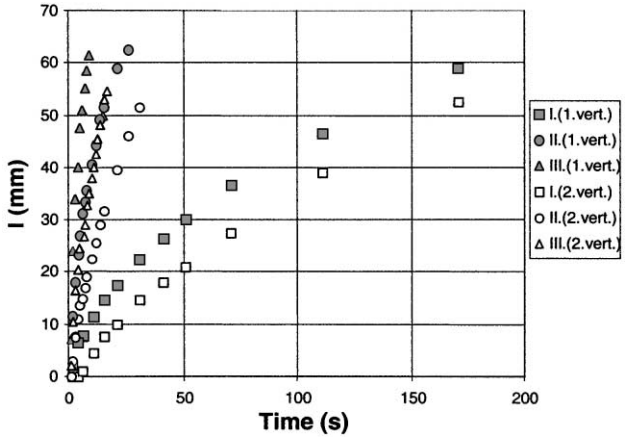

Fig. 20. The difference in reaction propagation between first and second vertical channels for different flow rates of ammonia.

Figs. 19 and 20 demonstrate the break of diagonal symmetry in propagation of the coloring reaction zone when the ammonia flow rate is increased from 5.5 to 49.4 $cm^3\ min^{-1}$. With the increase of the ammonia flow rate the propagation of the reaction zone along the first vertical channel is becoming much faster than the propagation of the reaction zone along successive vertical channels.

6. Analysis of heat generation within PWAFC

At low reactant gas flow rates the gas is uniformly distributed over the entire electrode surface. The current density is low and so is the Joule heat generated by electrolyte resistivity. The flow rate of the electrolyte is high enough to wet the entire inert matrix. The pressure drop

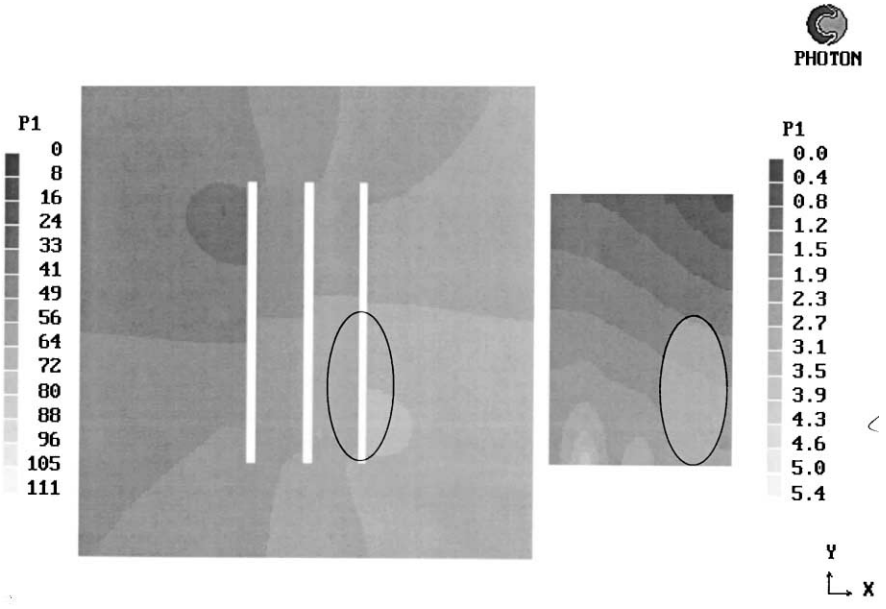

Fig. 21. A critical region of high heat generation in the PWAFC (ellipse) on cathode (left) and on matrix (right).

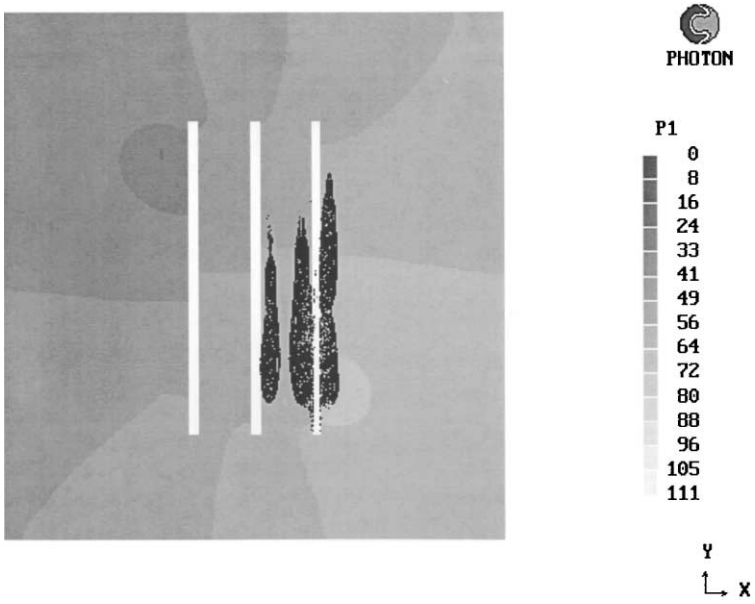

Fig. 22. Superposition of the photocopied damaged zone after post-mortem PWAFC analysis on the gas pressure distribution on the backside of the cathode obtained with the numerical simulation of the PWAFC.

due to reactant gas flow is lower than the bubble pressure of the electrolyte in the matrix and no reactant gas crossover occurs.

When the reactant gas flow rate increases, the heat load in the fuel cell increases due to higher current densities involved and due to higher rate of Joule heat generated. Moreover, the gas pressure drops become higher and the gas is non-uniformly distributed over the electrode surface. If the local mismatch between the gas and electrolyte flows is created, the locally generated heat can cause the electrolyte to dry. The solid crystalline electrolyte is permeable for the reactant gas (especially hydrogen) and crossover becomes possible. The hot spots are created within the cathode catalyst layer that can locally melt the PTFE and burn the catalyst. This would lead to the lower fuel cell efficiency and finally to the fuel cell break down. Based on the results of the numerical simulation of the reactant gas and electrolyte flows explained in Sections 4.1 and 4.2 and according to Fig. 15, one can expect that the critical region of the PWAFC be in its lower right corner (looking from cathode side). Here, the gas pressure is highest and the circulation of liquid electrolyte through the matrix is low, as shown in Fig. 21.

In few cases, as explained in the introduction, we have observed, after post-mortem analysis of the PWAFC, that the cathode, anode and matrix were melted together. The melted zone was repeatedly observed in the lower right region of the matrix and electrode assembly (looking from the cathode side). If this picture is superposed on the picture of stationary pressure distribution on cathode (Fig. 22), one can see that the damaged zone corresponds to the high gas pressure on the electrode and to the relatively low pressure of the electrolyte, exactly with the zones in Fig. 21, delineated by ellipse.

The explanation that the observed damages are the consequence of bad construction of gas and electrolyte distributors and not the consequence of cracks in the electrode catalyst layer is even more evident when the superposition of the damaged zone is made on the picture of the whiteprint paper coloring reaction propagation measured with the highest flow rate of ammonia (Fig. 23). The observed coincidence leaves no doubts about the usefulness and powerfulness of the CFD modeling in the design of the fuel cell.

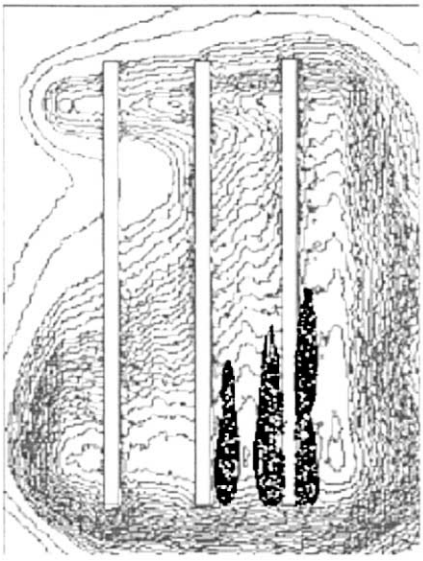

Fig. 23. Superposition of the photocopied damaged zone after post-mortem PWAFC analysis on the propagation contours of the whiteprint paper coloring reaction at highest ammonia flow rate.

7. Conclusions

The CFD study of the mass and heat transfer in the PWAFC enabled us to improve the design of the fuel cell in order to achieve as uniform as possible the reactant gases lateral distribution on the electrodes and heat generation. This is important because the ratio between the lateral electrode dimension (in *X*- or *Y*-axis direction) and the thickness of the matrix and electrode assembly is over 50. The results have undoubtedly pointed at changes to be made in the following details of PWAFC construction:

- The results of numerical simulation as well as the results of experiments with ammonia flow in the cathode compartment have revealed that the existing geometry of the distribution channels for gas and electrolyte in the PWAFC is not proper. Due to mismatch of electrolyte and gas flows the excess heat is generated in some critical points which lie around the gas inlet point, even when the fuel cell works at low power. When the power increases this phenomenon becomes more expressive. The damages appear locally, like that shown in Fig. 22, which lower the efficiency of the fuel cell. In order to avoid this, the step-like profile of the gas inlet channels must be eliminated, although this means the introduction of an additional layer and the increase of the fuel cell thickness.
- The cross-section of the horizontal channels must be increased in order to diminish the pressure drop along them.
- The inlet and outlet of gases and electrolyte must be provided from both sides of the horizontal channels in order to eliminate the diagonal distribution of gas and electrolyte on the electrode surface and within the matrix, respectively.
- The tightness of the fuel cell must be improved in order to prevent mixing of electrolyte and gas flow paths.
- The liquid cooling system must be introduced into the fuel cell stack design. In order to keep the temperature changes of PWAFC at peak power conditions within the limits of 7–9°C, we would need the mass flow of cooling water equal to 0.11 kg min^{-1} per cell. At normal working conditions of PWAFC (current density about 0.3 A cm^{-2}) the mass flow of water needed would be 4.7 times lower.

Acknowledgements

The financial support of the Ministry of Science and Technology (MZT) through the Grant J2-7500 is gratefully acknowledged. The authors are also grateful to the Ministry of Science and Technology of the Republic of Slovenia and to the Ministry of University and Scientific Research and Ministry of Foreign Affairs of the Republic of Italy for the financial support of the bilateral project ‘‘Low Temperature Fuel Cells’’.

References

[1] N. Giordano, P. Staiti, S. Hočevar, A.S. Aricò, Electrochim. Acta 41 (1996) 397–403.
[2] N. Giordano, P. Staiti, S. Hočevar, Z. Poltarzewski, Italian Patent MI 94 A 001980 (April 1994).
[3] O. Nakamura, T. Kodama, I. Ogino, Y. Miyake, Chem. Lett. (1979) 17.
[4] O. Nakamura, I. Ogino, T. Kodama, Solid State Ionics 3/4 (1981) 347.
[5] O. Nakamura, I. Ogino, Mater. Res. Bull. 17 (1982) 231.
[6] N. Giordano, P.L. Antonucci, S. Hočevar, Z. Poltarzewski, P. Staiti, in: Proceedings of the Fall Meeting of the Electrochemical Society, Extended Abstracts, Abstract no. 481, Vol. 90-2, Seattle, Washington, 14–19 October 1990, p. 701.
[7] P. Staiti, A.S. Aricò, S. Hočevar, V. Antonucci, J. New Mater. Electrochem. Syst. 1 (1998) 1–6.
[8] B. Keita, L. Nadjo, J. Electroanal. Chem. 269 (1989) 447.
[9] E.G. Zhizhina, L.I. Kuznetsova, R.I. Maksimovskaya, S.N. Pavlova, K.I. Matveev, J. Mol. Catal. 38 (1986) 345.
[10] B. Keita, L. Nadjo, J. Electroanal. Chem. 243 (1988) 87.
[11] N. Giordano, P. Staiti, A.S. Aricò, E. Passalacqua, L. Abate, S. Hočevar, Electrochim. Acta 42 (11) (1997) 1645–1652.
[12] S. Hočevar, E. Passalacqua, M. Vivaldi, A. Patti, N. Giordano, Electrochim. Acta 41 (18) (1996) 2817–2827.
[13] S. Srinivasan, O.A. Velev, A. Parthasarathy, D.J. Manko, A.J. Appleby, J. Power Sources 36 (1991) 299.
[14] A. Baumann, S. Hauff, K. Bolwin, J. Power Sources 36 (1991) 185–199.
[15] G. Maggio, V. Recupero, C. Mantegazza, J. Power Sources 62 (1996) 167–174.
[16] W. He, Q. Chen, J. Power Sources 55 (1995) 25–32.
[17] A.A. Kulikovsky, J. Divisek, A.A. Kornyshev, J. Electrochem. Soc. 146 (1999) 3981–3991.
[18] S. Dutta, S. Shimpalee, J.W. Van Zee, J. Appl. Electrochem. 30 (2000) 135–146.
[19] J.S. Yi, T.V. Nguyen, J. Electrochem. Soc. 146 (1999) 38–45.
[20] A. Kazim, H.T. Liu, P. Forges, J. Appl. Electrochem. 29 (1999) 1409–1416.
[21] P. Martin, ASHRAE J. January (1999) 20–25.
[22] PHOENICS Reference Manual, Version 2.2, Concentration, Heat & Momentum Limited (CHAM), London, 1998.
[23] F.P. Incropera, D.P. De Witt, Fundamentals of Heat and Mass Transfer, Wiley, New York, USA, 1990.
[24] Toray carbon paper TGP 090 characteristics, Toray Europe Ltd., London, 1996.
[25] CRC Handbook of Chemistry and Physics, 73rd Edition, CRC Press, Boca Raton, 1993, pp. 12–143.
[26] Fuel Cells: A Handbook (Revision 3), US Department of Energy, Office of Fossil Energy, Morgantown Energy Technology Center, Morgantown, WV, January 1994.
[27] Premiere Limited Edition, Reference Manual, Adobe.
[28] Micrografx Picture Publisher, Version 6.0 for Windows 95, Richardson, ZDA, September 1995.